Proceedings of the Combustion Institute 40 (2024) 105332

Contents lists available at ScienceDirect

Proceedings of the Combustion Institute

journal homepage: www.elsevier.com/locate/proci

Structure and dynamics of hexagonal cells in H_2/CO_2 flames

Thorsten Zirwes [a,*], Sven Eckart [b], Feichi Zhang [c], Thomas L. Kaiser [d], Kilian Oberleithner [d], Oliver T. Stein [e], Henning Bockhorn [e], Andreas Kronenburg [a]

[a] Institute for Combustion Technology (ITV), University of Stuttgart, Pfaffenwaldring 31, 70569 Stuttgart, Germany
[b] Institute of Thermal Engineering, TU Bergakademie Freiberg, Akademiestraße 6, 09599 Freiberg, Germany
[c] Institute for Technical Chemistry, Karlsruhe Institute of Technology, Kaiserstr.12, 76131, Karlsruhe, Germany
[d] Laboratory for Flow Instabilities and Dynamics, Institute of Fluid Dynamics and Technical Acoustics, Technische Universität Berlin, Müller-Breslau-Straße 8, 10623 Berlin, Germany
[e] Engler-Bunte Institute, Karlsruhe Institute of Technology, Engler-Bunte-Ring 7, 76131 Karlsruhe, Germany

ARTICLE INFO

Keywords:
Hexagonal flames
Hydrogen combustion
Cellular instabilities
Resolved numerical simulations
Laminar flames

ABSTRACT

Transition from fossil fuels to sustainably produced hydrogen remains an important goal to achieve current climate targets. Hydrogen from gasification and steam reforming is produced alongside CO_2. Instead of separating the CO_2, it can be kept in the product gas, leading to possible reductions in NO_x and improved safety aspects. However, the addition of CO_2 makes hydrogen flames more prone to cellular instabilities, which can lead to problems when designing burners for hydrogen-based flames. To understand the formation and dynamics of these instabilities, fully resolved 3D simulations of H_2/CO_2 cellular flames on a heat flux burner are performed. The numerical configuration follows an experimental setup that observed cellular and band-like structures stabilizing on the burner plate. With the simulations employing finite rate chemistry and detailed diffusion models, hexagonal flame structures are identified and characterized. The simulations show good qualitative agreement of the flame structure with the measurements. The influence of mass flow rate, burner plate temperature and equivalence ratio on the flame structure is investigated. A transition from band-like to hexagonal structures is described in terms of cusp formation, which become the corner points of the hexagonal cells, and the stabilization mechanism is explained via the high local flame stretch above holes in the burner plate. A Markstein number-based correlation for the cell size with respect to the burner plate temperature is proposed and the simulation data is provided as a public database for further analysis.

1. Introduction

In order to reach current carbon dioxide emission goals, a drastic shift from fossil fuels toward fuels from sustainable production has to be made. One promising fuel for our future energy landscape is hydrogen. However, compared to conventional hydrocarbon fuels, hydrogen is characterized by higher flame speeds due to its low molecular weight and therefore high diffusivity. As a consequence, preferential diffusion effects become important and thus lean hydrogen flames are prone to form thermodiffusive instabilities [1] with characteristic local extinction [2–4]. These instabilities can also be observed as polyhedral flames [5,6] and in tubular burners [7].

The theoretical description of flame instabilities is well established in terms of asymptotic theory and linear stability analysis. A robust framework has been developed by Matalon [8] that allows to predict the growth rate of instabilities at specific wave numbers and takes Darrieus–Landau and thermodiffusive instabilities into account. More recently, Berger et al. [9] compared the predictions from the theory to DNS of thermodiffusively unstable hydrogen flames and found good agreement for some conditions, but significant deviations for others, especially in terms of pressure dependence.

Steam reforming and gasification are possible paths for sustainable hydrogen production. These processes produce hydrogen alongside carbon monoxide (CO) and carbon dioxide (CO_2). Instead of separating CO_2 from the product mixture, it can be kept in the product gas. In this way, CO_2 serves as thermal diluent, reducing the flamespeed of the hydrogen flame, which reduces thermal NO_x emissions and improves safety relevant aspects of handling hydrogen [10]. However, CO_2 dilution also decreases the Lewis number of the gas mixture,

* Corresponding author.
E-mail addresses: thorsten.zirwes@itv.uni-stuttgart.de (T. Zirwes), Sven.Eckart@iwtt.tu-freiberg.de (S. Eckart), feichi.zhang@kit.edu (F. Zhang), t.kaiser@tu-berlin.de (T.L. Kaiser), oberleithner@tu-berlin.de (K. Oberleithner), oliver.t.stein@kit.edu (O.T. Stein), henning.bockhorn@kit.edu (H. Bockhorn), andreas.kronenburg@itv.uni-stuttgart.de (A. Kronenburg).

https://doi.org/10.1016/j.proci.2024.105332
Received 5 December 2023; Accepted 4 June 2024
Available online 24 June 2024

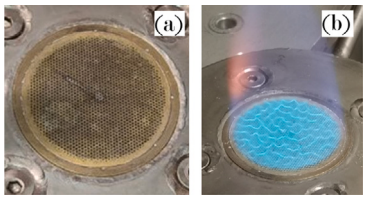

Fig. 1. (a) Closeup of the burner plate. (b) Cellular flame stabilizing above the burner plate.

whereby even stoichiometric to rich hydrogen flames diluted with CO_2 become thermodiffusively unstable [11].

Mixtures of H_2 and CO_2 were recently experimentally assessed by Eckart et al. [11] in a heat flux burner setup. With high CO_2 dilution, laminar flame speeds cannot be measured for most operating conditions because the flames form cellular structures on the burner plate. These types of cellular structures on porous burner plates have been observed before. Konnov et al. [12] studied methane and propane flames including CO_2 dilution [13] and found that the number of cells stabilizing on the burner plate strongly depends on the equivalence ratio. Jin et al. [14] studied hydrogen/methane/CO_2 flames with a McKenna burner. OH-PLIF was used to detect the structure of the cells forming on the burner plate and a strong dependence of cell size on equivalence ratio was found as well. Jiang et al. [15] confirmed the strong dependence of cell size on equivalence ratio in n-butane flames, but their measurements found only a weak dependence on flow velocity. Similar trends were also found by Katsumi et al. [16].

While the aforementioned works have investigated cellular structures on porous burner plates experimentally, a detailed description of flame structure is still missing. Because of this, the goal of this work is to conduct fully resolved 3D simulations of these types of flames. Simulations of this phenomenon are challenging because the flame structure is inherently three-dimensional and requires the full resolution of the flame front as well as the use of detailed chemical mechanisms and diffusion models. The timescales on which the cellular structures establish are of the order of seconds, making the simulations computationally demanding. To the best knowledge of the authors, this is the first time that cellular structures stabilized on burner plates are fully captured in numerical simulations. The simulations follow the experimental setup by Eckart et al. [11] and focus on CO_2 diluted hydrogen flames due to their technical importance for future hydrogen production.

2. Experimental and computational setup

2.1. Experimental setup

The setup used in the measurements is a heat flux burner for gaseous and liquid fuels with a burner plate diameter of 30 mm, shown in Fig. 1a. The plate can be heated up to 473 K and consists of 1519 holes with a diameter of 0.5 mm through which the premixed hydrogen–CO_2–air mixture flows. While this setup is usually used to measure laminar flame speeds, the cellular structures forming on the burner plate for large CO_2 dilution (shown in Fig. 1b) makes this impossible. Instead, an intensified camera was mounted above the heat flux burner to study the cellular structures by recording OH chemiluminescence in the range of 310 nm±8 nm. Since the focus of this work lies on the numerical simulations, we kindly refer the reader to [11,17,18] for more details about the experimental setup.

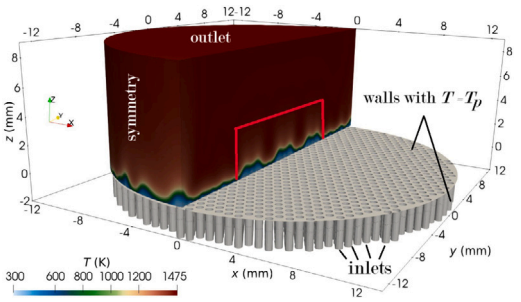

Fig. 2. Computational setup showing the burner plate, channels connecting the inlets to the holes in the plate, and cylindrical domain where the flame stabilizes, illustrated with the aid of the temperature field. T. The section marked in red is later discussed in Fig. 6.

2.2. Numerical setup

Preliminary studies have shown that the burner plate including all holes has to be considered in the simulations in order for the cellular structures to stabilize correctly. Therefore, the computational mesh has been built from the CAD data of the burner plate from the experimental setup. Fig. 2 shows the simulation domain: At the bottom, the burner plate can be seen. Each hole in the burner plate is connected to a fully resolved channel with a length of 2 mm, corresponding to the burner plate thickness, which serve as the inlets for the hydrogen–CO_2–air mixtures. Compared to the experiments, the radius of the burner plate has been reduced from 15 mm to 13 mm in the numerical setup to reduce simulation times. Above the burner plate, a cylindrical domain with a height of 9 mm is considered. In Fig. 2, the cylindrical domain is cut in half to show the holes in the burner plate in the foreground and the temperature field of the gas phase in the background.

The fresh gas enters the inlets at the bottom of each channel with a prescribed equivalence ratio ϕ and a temperature of 30 °C at atmospheric conditions. The fuel composition is given by hydrogen (35 vol-%) diluted with CO_2 (65 vol-%) and the oxidizer is air. This specific mixture was chosen because it represents typical gas compositions for hydrogen produced from low-grade biomass and used in integrated gasification combined cycle turbines. In the experimental setup, the burner plate is actively temperature controlled. Thermocouples placed in the plate showed temperature variations across the plate of 5 K. Therefore, the temperature of the channel walls and the burner plate is fixed at T_p. For all cases, the gas enters the plate at 30 °C and is then preheated while flowing through the burner plate to the plate temperature T_p. In this way, the amount of preheating can be varied while keeping the mass flow rate constant. The lateral surface of the cylindrical domain is a symmetry boundary condition to ensure overall adiabatic conditions and no flow recirculation from the surroundings. The top face of the cylindrical domain is an outlet. The hex-dominant mesh consists of an equidistant region with $\Delta x = 0.05$ mm for $z < 3$ mm. Due to the strong CO_2 dilution, the flame thickness of the hydrogen flames is increased, and all flames are resolved by 12–30 cells per thermal flame thickness, depending on the operating condition (equivalence ratio and burner plate preheating). Above $z > 3$ mm, only exhaust gases are present and the mesh resolution drops to $\Delta x = 0.1$ mm, with a total of about 20 million cells. Simulations are run until $t = 3$ s with a CFL number of 0.3, which corresponds to a time step of $(0.7-3)\times10^{-6}$ s, to ensure the full development of the cellular structures. A table summarizing the operating conditions and corresponding flame properties is included as supplementary material.

The simulations were conducted with the in-house code `EBIdnsFOAM` [19,20], which uses the finite volume method to solve the fully compressible Navier–Stokes equations, including buoyancy. All spatial derivatives are discretized by fourth order interpolation schemes and

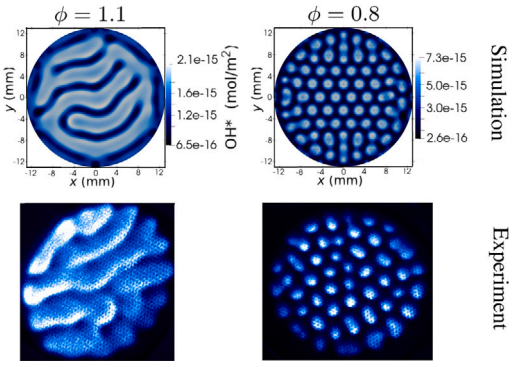

Fig. 3. Line-of-sight integrated OH* concentration from simulation (top) and measured OH* chemiluminescence (bottom) for $\phi = 1.1$ (left) and $\phi = 0.8$ (right).

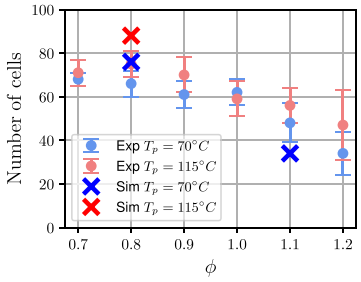

Fig. 4. Number of cells on the burner plate evaluated from the experiments and simulations.

an implicit second order backward scheme is used for temporal discretization. The mixture-averaged diffusion model (Curtiss–Hischfelder approximation) is used to compute molecular transport coefficients and the finite rate chemistry model is employed to compute the chemical reaction rates based on the DRM19 reaction mechanism [21]. This mechanism was chosen due to its relatively small size but good prediction quality for flame speeds and Markstein numbers (which are discussed later in the paper) of H_2/CO_2 mixtures used in this work (see [11] for mechanism validation).

3. Results and discussion

3.1. Comparison with measurements

In order to provide a qualitative comparison between the simulations and measurements, selected operating conditions were simulated with additional reactions for OH* [22]. Fig. 3 at the top shows line-of-sight integrated OH* concentrations from the simulation looking from the top toward the burner plate in the negative z direction. On the bottom, the OH chemiluminescence signal from the measurements is shown for two corresponding cases at $\phi = 1.1$ (left) and $\phi = 0.8$ (right). In general, two flame configurations can be observed in the experiments: a band-like structure at low mass flow rates, and a cellular structure at higher mass flow rates. Comparison between the measurements and simulations shows a good qualitative agreement, and the simulation is able to predict the correct shape and size of the cells. Note that the structures toward the burner edges might look different, due to the use of symmetry boundary conditions in the simulation, while the burner is open in the experiment.

To provide a quantitative comparison with the measurements and to validate the numerical setup, the number of cells on the burner plate formed by the flame has been evaluated. Fig. 4 compares the measured cell number with steady-state results from the simulations at varying equivalence ratios and burner plate temperatures. The measurements focused on varying the equivalence ratio, while the simulations focus on varying the mass flow rates and preheat temperatures. Note that the cell number from simulations is multiplied by a factor of $A_{\text{plate}}/A_{\text{plate,sim}} = 1.33$ to account for the different burner plate radii. For the available data points, trends are qualitatively captured correctly by the simulation and cell sizes agree well quantitatively, especially for $\phi = 0.8$.

3.2. Flame structure

As mentioned before, two configurations can be observed in the experiments: the hexagonal cellular structure, or a band-like structure. To see the transition between these states, a simulation was conducted where the mass flow rate is initially set to a value $\dot{m}_{\text{bulk}} = (1/A_0) \int \rho \boldsymbol{u} \cdot \boldsymbol{e}_z \, \mathrm{d}A = 0.21\,\mathrm{kg/m^2/s}$, where A_0 is the cross-sectional area, which is smaller than $\dot{m}_0 = s_L^0 \rho^0 = 0.29\,\mathrm{kg/m^2/s}$, where s_L^0 is the laminar flame speed and ρ^0 the density evaluated $T = T_p$. At these low mass flow rates, the flame is planar with strong heat losses to the burner plate. In the simulation, the mass flow rate is then increased linearly over time, as shown in Fig. 5 going from left to right and top to bottom. The flame is depicted by the temperature iso-surface of $T = 900\,\mathrm{K}$ colored by the OH mass fraction. An animation of this transition is available as supplementary material.

At first, single cells are blown off directly above one of the holes. Due to the thermodiffusive unstable behavior, the negative flame curvature at these points leads to lower local flame speeds so that the flame detaches from the burner surface at that point. At the same time, the surrounding flame gets enhanced by increasing positive flame stretch, eventually forming the troughs of the hexahedral structures. At $t = 0.8\,\mathrm{s}$, bands form above the burner plate in a striped horizontal pattern. The transition between the band structure and hexahedral cells occurs at about $\dot{m}/\dot{m}_0 = 2$. While this is currently only a numerical observation, it will be interesting to see if this applies to other cases and can be reproduced by the experimental setup. As the mass flow rate increases further, some of the bands begin to interact and merge. The points where the bands connect form cusps, which become the corner points of the hexahedral cells, as shown for $t > 1.7\,\mathrm{s}$.

The fully resolved simulations provide the opportunity to look into the structure of the flames stabilized on the burner plate. Fig. 6a shows the iso-surface of $T = 900\,\mathrm{K}$ colored by the OH mass fraction from the $\phi = 0.8$ flame in Fig. 3. The unburnt gas mixture is coming from below and the red dots on the surface are the effect of the jets exiting the holes in the burner plate. From the 3D rendering, it can be seen that the flame forms negatively curved ridges (blue regions with low OH) with cusps forming the corners of hexahedra. In this way, the cellular structures can be identified as hexagonal shapes, which will be discussed further below. Figs. 6b–d show different quantities on a 2D y-z cutting plane, marked as red box in Fig. 2. The subfigure on the bottom right, showing a top-down view of the hexagonal cells, shows the direction of the cut as a red line, i.e. the cutting plane passes through the ridges of the hexagonal cells.

Fig. 6b shows the temperature field on the cutting plane, Fig. 6c the heat release rate HRR and Fig. 6d the local equivalence ratio. The ridges of the hexagonal cells are where the flame is lifted from the burner plate, with the flame cusps forming the points of highest distance to the plate and lowest heat release rate. On the troughs, or positively stretched parts of the flame closest to the burner plate, the heat release rate is locally enhanced with slightly richer local equivalence ratios due to preferential diffusion, which is characteristic of thermodiffusively unstable flames [23–25]. The local enhancement lets the flame burn closer to the burner plate, stabilizing directly above one of the inlet holes, where the highest heat release rates are achieved.

Fig. 7 shows the structure of the bands, analogous to Fig. 6. It should be noted that the flame shown in Fig. 7 is not taken from the transient

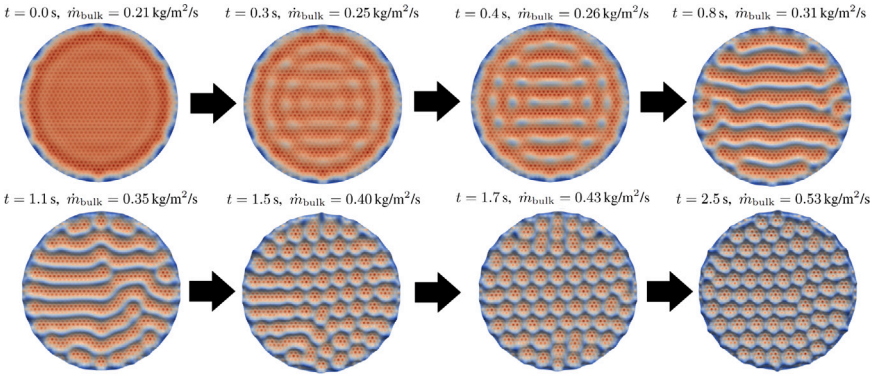

Fig. 5. Iso-surface of $T = 900\,\mathrm{K}$, colored by normalized OH mass fraction, for $\phi = 0.8$, $T_p = 115\ ^\circ\mathrm{C}$ and linearly increasing mass flow rate over time.

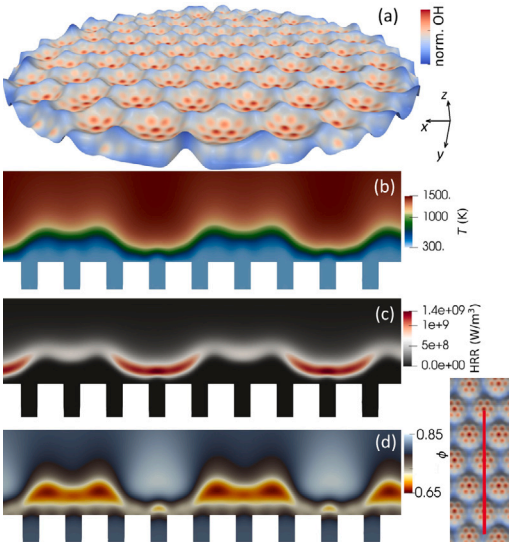

Fig. 6. (a) Iso-surface of $T = 900\,\mathrm{K}$ colored by normalized OH mass fraction. (b)–(d): temperature field, heat release rate and local equivalence ratio on a cutting plane, indicated by the subfigure on the bottom right. $\phi = 0.8$, $T_p = 115\ ^\circ\mathrm{C}$, $\dot{m}_{\mathrm{bulk}} = 0.46\,\mathrm{kg/m^2/s}$.

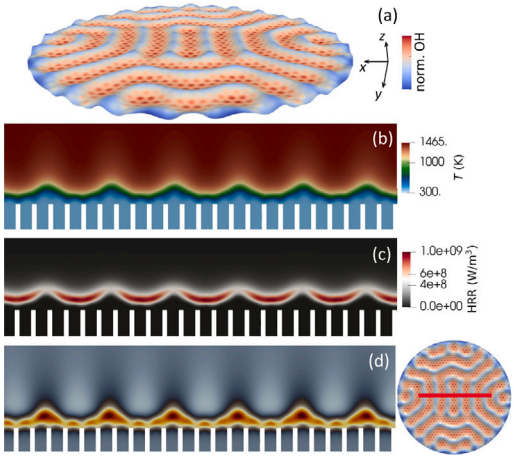

Fig. 7. (a) Iso-surface of $T = 900\,\mathrm{K}$ colored by normalized OH mass fraction. (b)–(d): temperature field, heat release rate and local equivalence ratio on a cutting plane, indicated by the subfigure on the bottom right. $\phi = 0.8$, $T_p = 115\ ^\circ\mathrm{C}$, $\dot{m}_{\mathrm{bulk}} = 0.31\,\mathrm{kg/m^2/s}$.

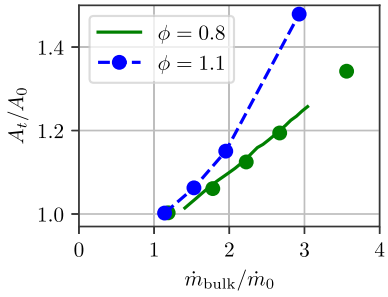

Fig. 8. Flame surface area normalized by cross-sectional area for $\phi = 0.8$, $T_P = 115\ ^\circ\mathrm{C}$ and $\phi = 1.1$, $T_p = 70\ ^\circ\mathrm{C}$.

simulation with increasing mass flow rate, but a simulation with fixed mass flow rate $\dot{m}_{\mathrm{bulk}} = 0.46\,\mathrm{kg/m^2/s}$, where a steady-state solution is achieved. In this solution, the bands form symmetric patterns on the burner plate. The structure of the band formation in Fig. 7 looks similar to the hexagonal cell structure in Fig. 6, with the difference that the cusps are less sharp and the flame stabilizes more closely to the burner plate due to the lower mass flow rate.

3.3. Effect of flow velocity

The effect of the flow velocity or mass flow rate is evaluated in Fig. 8 in terms of the flame surface area, measured by the iso-surface of $T = 900\,\mathrm{K}$. The green solid line shows the results from the transient simulation in Fig. 5. The green dots are simulations with fixed mass flow rate conducted until a steady-state solution is achieved, which shows that the mass flow rate in the transient simulation from Fig. 5 increases slowly enough so that the structures have time to form above the burner flame and relax to a quasi-steady state. The blue dots connected by dashed lines are steady-state simulation at $\phi = 1.1$ and a plate temperature of $T_p = 70\ ^\circ\mathrm{C}$. Here, a different T_p has been chosen so that both $\phi = 0.8$ and $\phi = 1.1$ flames are stable within a similar range of $\dot{m}_{\mathrm{bulk}}$. Below $\dot{m}_{\mathrm{bulk}}/\dot{m}_0 < 1$, the local flow velocity is effectively lower than the laminar flame speed and the flame is flat. Between $1 < \dot{m}_{\mathrm{bulk}}/\dot{m}_0 < 2$, the bands form on the burner plate and eventually lead to hexagonal cells for $\dot{m}_{\mathrm{bulk}}/\dot{m}_0 > 2$. The flame surface area increases approximately linearly with the mass flow rate, having slightly different slopes for the band-structure regime and hexahedral cell regime ($\dot{m}_{\mathrm{bulk}}/\dot{m}_0 < 2$) for $\phi = 1.1$.

The effect of the increasing mass flow rate on the flame structure is depicted in Fig. 9. The heat release rate on a cutting plane through the ridges of the hexagonal structures of the $\phi = 0.8$ flame is shown at two different mass flow rates. The increase in mass flow rate leads to a strong increase of local heat release rates at the positively stretched troughs of the cells and sharper cusps with slightly larger

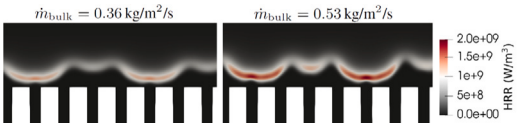

Fig. 9. Heat release rate on a $y-z$ oriented cutting plane through the ridges of the hexagonal cells for two different mass flow rates for the case with $\phi = 0.8$.

lift-off heights, which ultimately lead to larger flame surface area. However, in terms of the diameter of the cellular structures, the size stays nearly the same, as the increasing mass flow rate is balanced by more strongly stretched flame segments with larger local heat release rates. This explains why previous experimental studies did not find a strong dependence of cell size or cell number on flow velocity.

3.4. Effect of plate temperature

In order to study the effect of the plate temperature T_p, another transient simulation for the same case as before was conducted ($\phi = 0.8$, $\dot{m}_{\mathrm{bulk}} = 0.48\,\mathrm{kg/m^2/s}$) but at varying T_p. Fig. 10 shows the flame structure going from cold ($T_p = 30$ °C) to hot ($T_p = 190$ °C). The inlet temperature of the gas stays constant at 30°C. Similar to the case of varying mass flow rate, a transition between the hexagonal and band structures can be seen. Animations are available as supplementary material.

In terms of flame surface area, a similar trend is found as for the varying mass flow rate, i.e. a linear change of flame surface area with the plate temperature, as shown in Fig. 11.

In contrast to the varying mass flow rate, which has little effect on cell size, the diameter of the hexagonal structures changes between $30\ °\mathrm{C} \leq T_p \leq 110\ °\mathrm{C}$. Fig. 12 presents the structure of the hexagonal cells at $T_p = 35$ °C (left) and $T_p = 110$ °C (right). In contrast to the effect of varying mass flow rate, the change in burner plate temperature significantly alters the shape of the cells, leading to both larger cell diameters (compare the extend of the trough between the ridges in Fig. 12), as well as larger liftoff heights at lower plate temperatures.

The red line in Fig. 13 shows the cell diameter as a function of plate temperature for the case from Fig. 10. The cell diameter is evaluated by identifying the corner points of the hexagonal cells from the temperature iso-surface (red circles in the bottom left sub-figure of Fig. 13) and computing the hexagon diagonals. Only hexagonal cells within $r < 8$ mm are included in the evaluation to ensure that the results are independent of the influence of the outer boundary condition. The cell size decreases with increasing plate temperature. There is a jump between $T_p = 100$ °C and $T_p = 150$ °C, which likely is an artifact of the evaluation method, since the number of hexahedral cells is relatively low and thus the cell size is not statistically converged. However, the general trend is visible. At $T_p > 150$ °C, the band-like structures form, at which point the distance between bands is evaluated normal to the ridge direction. For T_p close to 200 °C, the bands become weak and a reliable evaluation of distances is not possible anymore.

The cellular structures on the burner plate exhibit typical properties of thermodiffusively unstable flames. An important dimensionless parameter for characterizing these flames is the Markstein number Ma. Ma measures how sensitive the flame reacts to flame stretch, which is important in the cellular structures due to the curved flame segments forming the ridges and tangential straining created by the jets coming from the holes in the burner plate. Formally, the Markstein number is defined as

$$Ma = -\frac{\partial s/s_L^0}{\partial Ka}, \tag{1}$$

where s is the local flame speed at a given flame stretch, s_L^0 is the laminar flame speed of the unstretched flame and Ka is the dimensionless flame stretch. As $Ma \to 0$, the flame becomes less sensitive to flame stretch, local curvatures do not affect local heat release rates or burning rates, so that the flame cannot form cellular instabilities anymore.

Table 1
Length scale from theory compared with distance between cusps from the simulation.

T_p (°C)	30	70	100
Theory (mm)	2.22	1.74	1.42
Simulation (mm)	1.86	1.73	1.58

The blue line in Fig. 13 shows the Markstein numbers for $\phi = 0.8$ as a function of T_p obtained from reference 1D stretched premixed counterflow twin flames computed with Cantera. As T_p increases and the gas mixture is preheated, the Markstein number approaches zero. As the Markstein number becomes closer to zero, the size of the cells decreases as well, because locally, burning rates are enhanced increasingly less at the troughs of the cells and high-curvature regions of the ridges cannot stabilize anymore. Instead, the flame surface area must increase to balance the mass flow rate by creating cells with smaller diameter. As the Markstein number becomes zero near $T_p = 190$ °C, the flame approaches a flat flame without exhibiting characteristics of thermodiffusively unstable flames.

Another way to analyze the size of the cell structures is to compare with predictions from linear stability analysis [8,9]. Since this setup is strongly affected by heat loss, application of stability analysis is challenging. Table 1 compares the length scale at the maximum dispersion rate with the average distance between two cell cusps from the simulation. Cell cusps are the points that are lifted the most from the burner plate and therefore are least affected by heat losses It should be noted that predictions from theory have been scaled down by a factor of 2π and it remains to be seen if this holds for other conditions as well. Additional information is included in the supplementary material.

3.5. Effect of equivalence ratio

As found by previous works, there is a strong dependence of the cell size on the equivalence ratio. However, due to the cost of each numerical simulation as well as the difficulty of stabilizing flames at varying ϕ but fixed $\dot{m}_{\mathrm{bulk}}$ and T_p, we present a brief discussion and outlook on this topic.

Fig. 14 at the top shows the iso-surface of $T = 900$ K, colored by the normalized OH mass fraction of three different equivalence ratios. It is evident that as ϕ increases, the cell size increases as well. We chose these specific conditions because they have similar Ma. This was achieved by varying the plate temperature, i.e. $T_p = 70$ °C for $\phi = 1.1$, $T_p = 115$ °C for $\phi = 0.8$ and $T_p = 150$ °C for $\phi = 0.9$ (in this case, the fuel composition for the $\phi = 0.9$ case is 70% CO_2 and 30% H_2). Even though each case has a similar Markstein number, the cell sizes are different.

The ratio of Markstein number magnitude and cell diameter is roughly $\mathcal{O}(0.1\,\mathrm{mm^{-1}})$, which might be used as a first order estimate for predicting the cell size as function of ϕ and T_p. It remains to be seen if this trend stays valid for different operating conditions and fuel types. As mentioned briefly before, simulations with $\phi = 0.8$ can generally be performed at fixed $\dot{m}_{\mathrm{bulk}}$ and T_p until steady-state conditions are reached. For $\phi = 1.1$, the hexagonal and band structures typically keep moving across the burner plate and do not reach a steady-state solution. This could be attributed to the larger cell size, making it harder to form a sufficient number of symmetric cells near the center of the domain given the constraint by the radius of the burner. At the same time, the Markstein number of $\phi = 1.1$ is closer to zero compared to $\phi = 0.8$ for the same T_p, which means that the $\phi = 1.1$ flame is less sensitive to flame stretch and can therefore not as easily anchor at the burner plate holes from local enhancement of flame speeds.

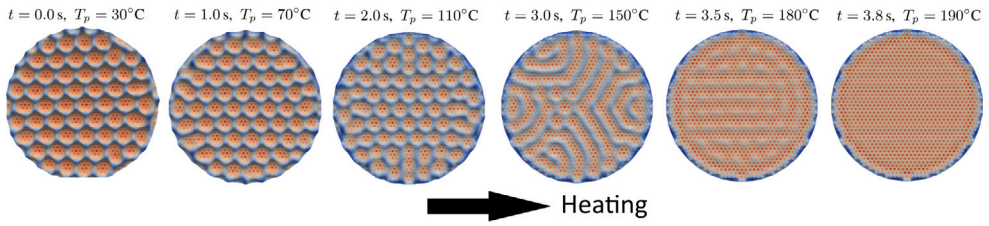

Fig. 10. Flame structure visualized as temperature iso-surface $T = 900\,\mathrm{K}$ colored by normalized OH mass fraction for $\phi = 0.8$, $\dot{m}_{\mathrm{bulk}} = 0.48\,\mathrm{kg/m^2/s}$ and varying T_p.

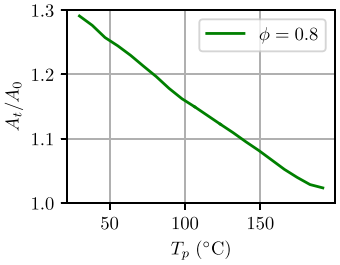

Fig. 11. Flame surface area determined from the iso-surface $T = 900\,\mathrm{K}$ for $\phi = 0.8$ at $\dot{m}_{\mathrm{bulk}} = 0.48\,\mathrm{kg/m^2/s}$ for varying T_p.

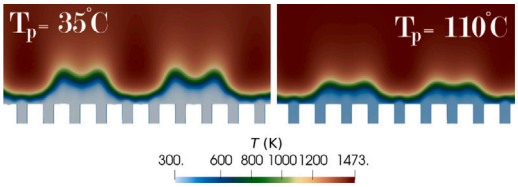

Fig. 12. Temperature on a $y-z$ oriented cutting plane through the ridges of the hexagonal cells for two different burner plate temperatures for the case with $\phi = 0.8$.

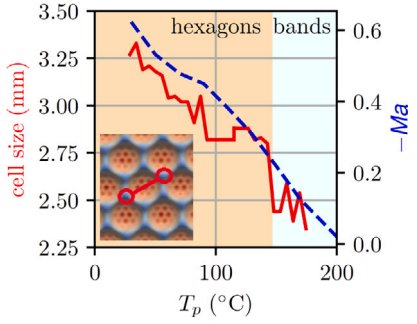

Fig. 13. Cell size evaluated from the band and hexagonal structures at varying T_p from the 3D simulation. Markstein numbers obtained from reference 1D counterflow twin flames computed for $\phi = 0.8$ as a function of T_p.

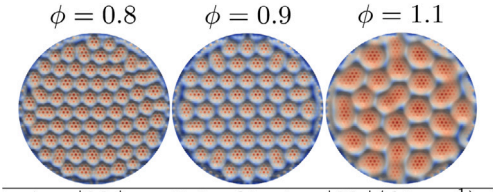

ϕ	$\lvert Ma\rvert$	cell size d (mm)	$\lvert Ma\rvert/d$ ($\mathrm{mm^{-1}}$)
0.8	0.40	3.0	0.13
0.9	0.41	3.7	0.11
1.1	0.44	5.5	0.08

Fig. 14. Iso-surface of $T = 900\,\mathrm{K}$ colored by OH mass fraction for three equivalence ratios. The table shows the Markstein number and cell size for the different cases.

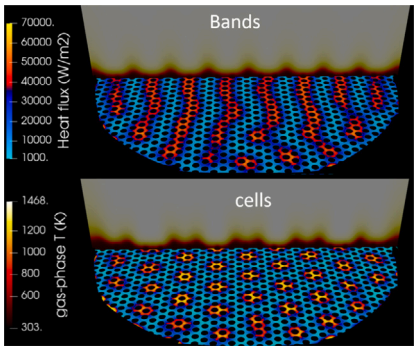

Fig. 15. Heat losses to the burner plate for band (top) and cell (bottom) structures along with a cutting plane showing gas-phase temperature.

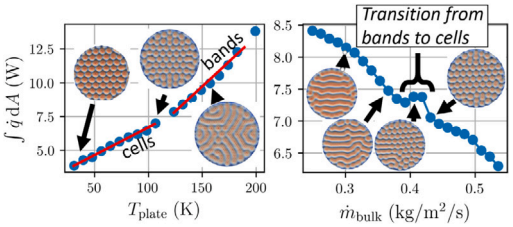

Fig. 16. Heat losses to the plate during regime transition.

3.6. Heat losses during regime transition

The heat losses of the flame to the burner plate have been evaluated from the simulation database. Fig. 15 shows the burner plate colored by heat flux $\dot{q}$, with a vertical cutting plane showing the gas-phase temperature. A case with band structures ($\phi = 0.8$, $\dot{m}_{\mathrm{bulk}} = 0.31\,\mathrm{kg/m^2/s}$) is shown at the top, and a case with cellular structures ($\phi = 0.8$, $\dot{m}_{\mathrm{bulk}} = 0.43\,\mathrm{kg/m^2/s}$) at the bottom. For the band structures, the overall area with large heat losses $\dot{q}$ is larger compared to the cell structures, while the cell structures show spots with locally higher $\dot{q}$.

Heat losses integrated over the whole burner plate $\dot{Q} = \int \dot{q}\,\mathrm{d}A$ for $\phi = 0.8$ are shown in Fig. 16 on the left for increasing T_p. As T_p (and thus pre-heating) increases, quenching distances decrease so that $\dot{Q}$ increases with T_p. It is interesting to note that the cell and band structures show different slopes due to the larger portion of flame surface being lifted from the plate for cellular structures. The plot on the right shows $\dot{Q}$ as a function of $\dot{m}_{\mathrm{bulk}}$. As $\dot{m}_{\mathrm{bulk}}$ increases, flames are lifted further from the burner plate, decreasing $\dot{Q}$. However, transition from band to cell structures can be observed by a local peak in $\dot{Q}$.

4. Summary and conclusions

This work presents the first fully resolved 3D simulations of cellular flames on flat-flame burners, revealing a hexagonal cell structure and transition to a band-like structure. Good agreement is achieved between simulations and measurements, both for hexagonal and band-like structures. The conclusions of this work are summarized as follows:

(i) The flame structure of the cellular flames shows the characteristics of thermodiffusively unstable flames, where large positive flame stretch directly above a hole in the burner plate leads to the stabilization of the trough of the cells.
(ii) When the band-like structures merge to hexagonal cells, points where the bands touch form the corner points (cusps) of the hexagonal cells.
(iii) Increasing flow speed enhances local flame stretch and thus local heat release rates in the troughs of the structures. However, cell diameters stay nearly constant.
(iv) In contrast, increasing the plate temperature leads to both a decrease in total flame surface area and cell size. At higher temperatures, Markstein numbers get closer to zero, so that the flame becomes less sensitive to stretch, leading to more cells instead of more pronounced cell structures with higher ridges and sharper cusps.
(v) The strong dependence of cell size on equivalence ratio from experiments in the literature is found by the simulations as well. A first order estimate of the cell size could be derived from the Markstein number.

The simulation database can be downloaded from https://github.com/g3bk47/HexagonalFlameCells to enable further in-depth evaluation of local flame dynamics.

Novelty and significance statement

To the best knowledge of the authors, this work provides the first fully resolved simulation of cellular structures on porous plate burner configurations, revealing a transition of band-like flame structures to hexagonal cells. Due to the use of finite rate chemistry and detailed diffusion models, the characteristic structure of thermodiffusively unstable flames is identified in the hexagonal structure and used to explain the stabilization process. The transition morphology from band-like structures to hexagonal cells is explored and the influence of mass flow rate and burner plate temperature is evaluated. We chose H_2/CO_2 mixtures as fuel due to their relevance in the sustainable production of hydrogen. The addition of CO_2 makes hydrogen flames more prone to thermodiffusive instabilities, which makes this setup well suited to explore the influence of operating conditions on the cellular structures. All simulation data will be made publicly available.

CRediT authorship contribution statement

Thorsten Zirwes: Software, Investigation, Writing – original draft. **Sven Eckart:** Investigation, Visualization, Writing – review & editing. **Feichi Zhang:** Resources, Conceptualization, Writing – review & editing. **Thomas L. Kaiser:** Investigation, Formal analysis, Writing – review & editing. **Kilian Oberleithner:** Investigation, Writing – review & editing. **Oliver T. Stein:** Investigation, Conceptualization, Writing – review & editing. **Henning Bockhorn:** Conceptualization, Supervision, Writing – review & editing. **Andreas Kronenburg:** Resources, Supervision, Writing – review & editing.

Declaration of competing interest

The authors declare that they have no known competing financial interests or personal relationships that could have appeared to influence the work reported in this paper.

Acknowledgments

Simulations were performed on the national supercomputer HPE Apollo Hawk at the High Performance Computing Center Stuttgart (HLRS) under the acronym dnsBomb and HoreKa under the acronym H2dns funded by the Ministry of Science, Research and the Arts Baden-Württemberg, Germany and DFG (“Deutsche Forschungsgemeinschaft”), Germany. The authors gratefully acknowledge the financial support by the Helmholtz Association of German Research Centers (HGF), within the research field Energy, program Materials and Technologies for the Energy Transition (MTET), topic Resource and Energy Efficiency and the financial support by the Deutsche Forschungsgemeinschaft, Germany (DFG, project number 439610422).

Appendix A. Supplementary material

Supplementary material related to this article can be found online at https://doi.org/10.1016/j.proci.2024.105332.

References

[1] L. Berger, A. Attili, H. Pitsch, Synergistic interactions of thermodiffusive instabilities and turbulence in lean hydrogen flames, Combust. Flame 244 (2022).
[2] C. Law, S. Ishizuka, P. Cho, On the opening of premixed bunsen flame tips, Combust. Sci. Technol. 28 (3–4) (1982) 89–96.
[3] T. Zirwes, F. Zhang, Y. Wang, P. Habisreuther, J.A. Denev, Z. Chen, H. Bockhorn, D. Trimis, In-situ flame particle tracking based on barycentric coordinates for studying local flame dynamics in pulsating bunsen flames, Proc. Combust. Inst. 38 (2021) 2057–2066.
[4] X. Wen, T. Zirwes, A. Scholtissek, H. Böttler, F. Zhang, H. Bockhorn, C. Hasse, Flame structure analysis and composition space modeling of thermodiffusively unstable premixed hydrogen flames–Part I: Atmospheric pressure, Combust. Flame (2021).
[5] H. Lulic, A. Breicher, A. Scholtissek, P.E. Lapenna, A. Dreizler, F. Creta, C. Hasse, D. Geyer, F. Ferraro, On polyhedral structures of lean methane/hydrogen bunsen flames: Combined experimental and numerical analysis, Proc. Combust. Inst. (2022).
[6] S. Shi, A. Breicher, J. Trabold, S. Hartl, R.S. Barlow, A. Dreizler, D. Geyer, Cellular structures of laminar lean premixed H2/CH4/air polyhedral flames, Appl. Energy Combust. Sci. 13 (2023).
[7] H.S. Bak, C.S. Yoo, Flame instabilities and flame cell dynamics in opposed nonpremixed tubular flames with radiative heat loss, Combust. Flame 194 (2018) 322–333.
[8] M. Matalon, Intrinsic flame instabilities in premixed and nonpremixed combustion, Annu. Rev. Fluid Mech. 39 (2007) 163–191.
[9] L. Berger, A. Attili, H. Pitsch, Intrinsic instabilities in premixed hydrogen flames: Parametric variation of pressure, equivalence ratio, and temperature. Part 1-Dispersion relations in the linear regime, Combust. Flame 240 (2022) 111935.
[10] G. Pio, A. Ricca, V. Palma, E. Salzano, Experimental and numerical evaluation of low-temperature combustion of bio-syngas, Int. J. Hydrogen Energy 45 (1) (2020) 1084–1095.
[11] S. Eckart, G. Pio, T. Zirwes, F. Zhang, E. Salzano, H. Krause, H. Bockhorn, Impact of carbon dioxide and nitrogen addition on the global structure of hydrogen flames, Fuel 335 (2022).
[12] A.A. Konnov, I.V. Dyakov, Experimental study of adiabatic cellular premixed flames of methane (ethane, propane) + oxygen + carbon dioxide mixtures, Combust. Sci. Technol. 179 (4) (2007) 747–765.
[13] A.A. Konnov, I.V. Dyakov, Measurement of propagation speeds in adiabatic cellular premixed flames of CH4+O2+CO2, Exp. Therm. Fluid Sci. 29 (8) (2005) 901–907.
[14] W. Jin, J. Wang, S. Yu, Y. Nie, Y. Xie, Z. Huang, Cellular instabilities of non-adiabatic laminar flat methane/hydrogen oxy-fuel flames highly diluted with CO2, Fuel 143 (2015) 38–46.
[15] L. Jiang, C. Gu, G. Zhou, F. Li, Q. Wang, Cellular instabilities of n-butane/air flat flames probing by PLIF-OH and PLIF-CH2O laser diagnosis, Exp. Therm. Fluid Sci. 118 (2020).
[16] T. Katsumi, T.T. Aung, S. Kadowaki, Instability phenomena of lean hydrogen/oxygen/inert-gas premixed flames on a flat burner, J. Vis. 25 (5) (2022) 1075–1083.
[17] S. Eckart, L. Pizzuti, C. Fritsche, H. Krause, Experimental study and proposed power correlation for laminar burning velocity of hydrogen-diluted methane with respect to pressure and temperature variation, Int. J. Hydrogen Energy 47 (9) (2022) 6334–6348.
[18] S. Eckart, I.G. Zsély, H. Krause, T. Turányi, Effect of the variation of oxygen concentration on the laminar burning velocities of hydrogen-enriched methane flames, Int. J. Hydrogen Energy (2023).

[19] T. Zirwes, M. Sontheimer, F. Zhang, A. Abdelsamie, F.E. Hérnandez Pérez, O.T. Stein, H.G. Im, A. Kronenburg, H. Bockhorn, Assessment of numerical accuracy and parallel performance of openFOAM and its reacting flow extension EBIdnsFoam, Flow Turb. Comb. (2023).
[20] T. Zirwes, F. Zhang, H. Bockhorn, Memory effects of local flame dynamics in turbulent premixed flames, Proc. Combust. Inst. 39 (2) (2022) 2349–2358.
[21] A. Kazakov, F. Frenklach, DRM19, 2019, http://combustion.berkeley.edu/drm/.
[22] T. Kathrotia, U. Riedel, A. Seipel, K. Moshammer, A. Brockhinke, Experimental and numerical study of chemiluminescent species in low-pressure flames, Appl. Phys. B 107 (3) (2012) 571–584.
[23] L. Berger, K. Kleinheinz, A. Attili, H. Pitsch, Characteristic patterns of thermodiffusively unstable premixed lean hydrogen flames, Proc. Combust. Inst. 37 (2) (2019) 1879–1886.
[24] H. Böttler, H. Lulic, M. Steinhausen, X. Wen, C. Hasse, A. Scholtissek, Flamelet modeling of thermo-diffusively unstable hydrogen-air flames, Proc. Combust. Inst. (2022).
[25] X. Wen, T. Zirwes, A. Scholtissek, H. Böttler, F. Zhang, H. Bockhorn, C. Hasse, Flame structure analysis and composition space modeling of thermodiffusively unstable premixed hydrogen flames–Part II: Elevated pressure, Combust. Flame (2021).